Available online at www.sciencedirect.com
ScienceDirect
Journal of Catalysis 249 (2007) 220–233
JOURNAL OF CATALYSIS
www.elsevier.com/locate/jcat

Location and coordination of promoter atoms in Co- and Ni-promoted MoS_2-based hydrotreating catalysts

Jeppe V. Lauritsen [a,*], Jakob Kibsgaard [a], Georg H. Olesen [a], Poul G. Moses [b], Berit Hinnemann [b,c], Stig Helveg [c], Jens K. Nørskov [b], Bjerne S. Clausen [c], Henrik Topsøe [c], Erik Lægsgaard [a], Flemming Besenbacher [a,*]

[a] *Department of Physics and Astronomy, Interdisciplinary Nanoscience Center (iNANO), University of Aarhus, DK-8000 Aarhus C, Denmark*
[b] *Department of Physics and Center for Atomic-Scale Materials Design (CAMD), NanoDTU, Technical University of Denmark, DK-2800 Lyngby, Denmark*
[c] *Haldor Topsøe A/S, Nymøllevej 55, DK-2800 Lyngby, Denmark*

Received 1 December 2006; revised 16 April 2007; accepted 17 April 2007

Available online 8 June 2007

Abstract

In this study, we used scanning tunneling microscopy (STM) and density functional theory (DFT) to investigate the atomic-scale structure of the active Co- or Ni-promoted MoS_2 nanoclusters in hydrotreating catalysts. Co-promoted MoS_2 nanoclusters (Co–Mo–S) are found to adopt a hexagonal shape, with Co atoms preferentially located at $(\bar{1}010)$ edges with a 50% sulfur coverage. The first atom-resolved STM images of the Ni-promoted MoS_2 nanoclusters (Ni–Mo–S) reveal that the addition of Ni also leads to truncated morphologies, but the degree of truncation and the Ni sites are observed to depend on the nanocluster size. Larger clusters (type A) are structurally similar to Co–Mo–S exposing fully Ni-substituted $(\bar{1}010)$ edges with a 50% S coverage. Smaller clusters (type B) show dodecagonal shapes terminated by three different edges, all of which contain Ni-promoter atoms fully or partially substituting the Mo atoms. The findings may shed more light on the different selectivities observed for the Co- and Ni-promoted hydrotreating catalysts.
© 2007 Elsevier Inc. All rights reserved.

Keywords: Hydrotreating; Hydrodesulfurization; Hydrodenitrogenation; HDS; Model catalyst; Scanning tunneling microscopy; STM; Molybdenum disulfide; MoS_2 nanoclusters; Morphology; Promoters; Ni–Mo–S; Co–Mo–S

1. Introduction

The catalytic removal of sulfur and nitrogen impurities from oil compounds by hydrotreating is a key process in modern industrial oil refining that is currently receiving considerable attention due to the increasing demand for clean fuels. To meet present and future requirements for fuels with low impurity levels, more active and selective catalysts are being requested by oil refineries [1–4]. Consequently, intense research efforts are being directed toward improving the MoS_2-based hydrotreating catalyst that have been widely applied in this area for more than half a century [5–7].

The commercial hydrotreating catalysts consist of promoted MoS_2 or WS_2 particles distributed on a high-surface area support, such as alumina. It is well established that the MoS_2 crystallites in typical high-activity catalysts are present as single-layer S–Mo–S slabs with an average size of 2–3 nm under operating conditions [5]. Furthermore, it is well established that Co or Ni added to the MoS_2 increases the reactivity of the catalysts, and because only a small fraction of Co or Ni relative to Mo is needed, they are considered *promoters* rather than catalysts in their own right. For both promoters, the overall hydrotreating activity generally increases by more than an order of magnitude, and the specific selectivities of the sulfided CoMo or NiMo catalysts change with respect to hydrodesulfurization (HDS), hydrodenitrogenation (HDN), and hydrogenation

* Corresponding authors.
E-mail addresses: jvang@inano.dk (J.V. Lauritsen), fbe@inano.dk (F. Besenbacher).

0021-9517/$ – see front matter © 2007 Elsevier Inc. All rights reserved.
doi:10.1016/j.jcat.2007.04.013

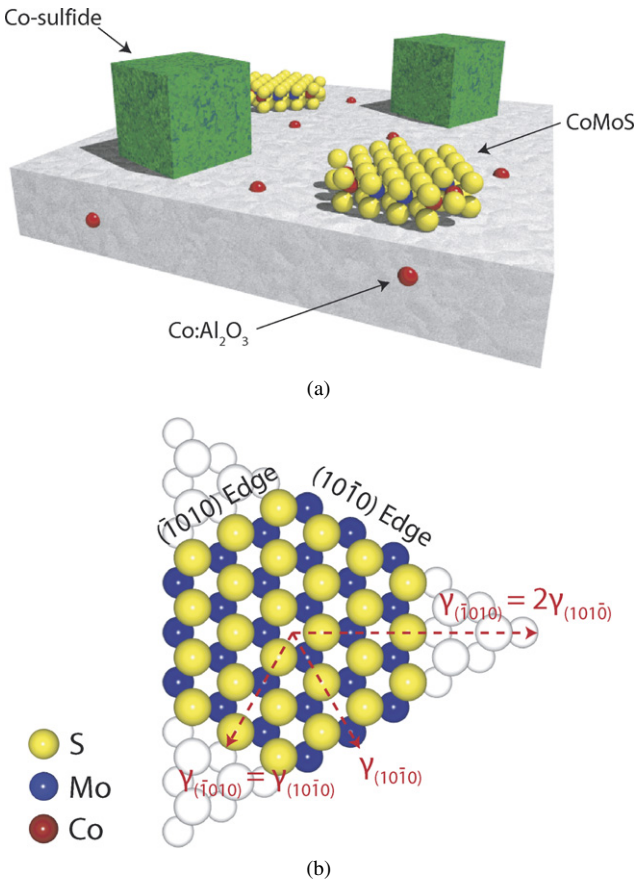

Fig. 1. (a) Illustration of the phases in a sulfided Co–Mo catalyst. (b) Ball model of a bulk-truncated, hypothetical hexagonal MoS_2 nanocluster exposing the (0001) basal plane.

(HYD). Thus, the effect of the two promoters may be quite different [5,8].

Many studies have been carried out to correlate the structure of the active promoted phases in catalysts to the reactivity [5, 9–17], and general consensus has been reached in the literature on the so-called "Co–Mo–S" model [5]. This model originates from the finding that Co atoms may be located at the edge positions of MoS_2 nanostructures [18,19], and the observations that the Co–Mo–S structures are responsible for the promotion of the reactivity [19,20]. Co is present in three different phases in the catalyst (Fig. 1a). The catalytically most interesting Co–Mo–S phase has an MoS_2-like texture, into which Co atoms are incorporated. Co–Mo–S is non-stoichiometric with respect to the Co/Mo ratio, and no unit cell can be defined in the crystallographic sense. For unpromoted MoS_2, it has long been known that only the edges, not the basal plane sites, are active [5,21,22], and thus it has been proposed that the Co atoms located at edge positions create new and more active sites by, for example, providing active sites in the form of sulfur vacancies at or next to the Co sites [18,19,23,24]. But the exact origin of the promoting role of Co remains a matter of intense debate, since most analysis tools provide only indirect evidence of the location of Co in Co–Mo–S structures [12,25–28]. Fewer structural studies have been performed for the Ni-promoted system [29–31]. It is generally believed that a Ni–Mo–S phase exists with a structure similar to Co–Mo–S, but no direct experimental information is available on the location of the Ni promoters on Ni–Mo–S. Theoretical studies based on slab models [32–37] or calculations of cluster structures [38] have been used to investigate the affinities for Co or Ni to replace Mo at the MoS_2 edges, and such studies have also provided information on the sulfur coverage at the edges under experimental and reaction conditions.

Recently, we used high-resolution scanning tunneling microscopy (STM) to investigate the atomic-scale structure of MoS_2 and Co–Mo–S nanoclusters on a gold [39–42] or a graphite model substrate [43]. The main advantage of using STM to study model catalysts is that it provides real-space, atom-resolved microscopy images of the individual nanoclusters, making it possible to resolve some of the above-mentioned important questions related to the detailed structure and morphology of the Co–Mo–S and Ni–Mo–S nanoclusters. In particular, the present study has provided the first experimental microscopy images of single Ni promoter atoms in Ni–Mo–S, along with theoretical support for previous STM studies of Co–Mo–S clusters [39]. Interestingly, we observed significant differences in the morphology and atomic-scale structure of Ni–Mo–S compared with Co–Mo–S; such insights may provide the basis for a better understanding of the differences in activity and selectivity in the two promoted systems. This insight may also shed more light on the observation that direct desulfurization (DDS) and HYD routes in HDS are not always inhibited in the same way in Ni–Mo–S as in MoS_2 or Co–Mo–S in the presence of nitrogen-containing compounds [7, 44,45]. This is explained in terms of competitive adsorption on the sites responsible for sulfur extrusion or HYD. We have previously shown that metallic brim states at the edges of unpromoted MoS_2 nanoclusters are active as HYD sites [42,46], whereas sulfur vacancies formed at the edges are active in direct sulfur extrusion. Interestingly, we observed in this study several metallic edge states in the promoted clusters as well, and, given the potential importance of these in HYD reactions, we have provided a thorough electronic structure characterization of these metallic edge states in both Co–Mo–S and Ni–Mo–S.

2. Methods

2.1. Experimental details

The experiments were performed in an ultra-high vacuum (UHV) chamber equipped with standard surface analysis equipment and equipment for depositing refractory metals by *e*-beam evaporation and for introducing high-purity gases to the chamber. The homebuilt Aarhus scanning tunneling microscope [47] was used for the experiments.

As demonstrated in previous studies for the unpromoted MoS_2 model catalysts [40–42] and the first studies of Co–Mo–S [39], a single crystal Au(111) surface can be used as a suitable model substrate to synthesize highly dispersed ensembles of Co–Mo–S or Ni–Mo–S nanoclusters. Recently, the same surface was used to synthesize other supported sulfide nanostructures [48,49]. STM studies have shown that a graphite

(HOPG) substrate also can be used [43] for the synthesis of MoS_2 nanoparticles and the edge structure of the supported MoS_2 nanoclusters was observed to be identical to MoS_2 supported on gold. But in these studies, the Au(111) substrate was preferred, because it exposes the characteristic herringbone reconstruction [50], providing a regular array of nucleation sites for metal atoms and thereby facilitating a high dispersion of submonolayer amounts of Mo, Ni, or Co into nanoclusters [40,51–53]. The Au(111) single crystal surface was prepared by cycles of Ar^+ sputtering, followed by annealing at 900 K for 10 min. This procedure generated a clean and regular Au(111) surface, as judged by Auger electron spectroscopy (AES) and STM. For the synthesis of Co–Mo–S and Ni–Mo–S nanoclusters, the pure metals were evaporated onto the substrate using an *e*-beam evaporator (Oxford Applied Research, EGCO-4).

Using the approach described in Ref. [39] as the starting point, we investigated a number of synthesis procedures for formation of the mixed phases of both the Ni- and Co-promoted MoS_2 nanoclusters. Using the procedure to form unpromoted MoS_2 nanoclusters as described in Refs. [40,54] and subsequently deposit Co or Ni in a sulfiding atmosphere of 10^{-6} mbar of H_2S, we found that this approach did not lead to the spontaneous formation of bimetallic sulfided structures. Instead, well-separated MoS_2 nanoclusters and cobalt-sulfide or nickel-sulfide patches could be identified in atom-resolved STM images. The bimetallic Co–Mo–S and Ni–Mo–S nanoclusters could be formed when Mo was simultaneously deposited together with Co or Ni, respectively, in the sulfiding atmosphere of 10^{-6} mbar of H_2S. This step was followed by postannealing at temperatures of 673 K while maintaining the sulfiding atmosphere to further crystallize the nanoclusters. The most efficient method involved deposition of Mo onto the Au(111) surface in a sulfiding atmosphere to form sulfided Mo embryos, followed by co-deposition of additional Mo together with Ni or Co to form a capped layer of bimetallic sulfide. The total coverages in all experiments were calibrated before the S exposure and were estimated to be $10 \pm 1\%$ of a monolayer (ML) for Mo and $4 \pm 1\%$ ML for Ni and Co.

2.2. Computational details

The theoretical calculations were based on DFT using the generalized gradient approximation for the exchange-correlation part of the total energy functional. The edges of single-layer MoS_2 particles were investigated using a model consisting of semi-infinite slabs of MoS_2 repeated in a supercell geometry, as reported in [32,54,55]. The stripes used for the calculations in this work were composed of repeat units containing one or two MoS_2 units. Each supercell exposed the $(\bar{1}010)$ edge at one edge and the $(10\bar{1}0)$ edge at the other. The edges were separated by six unit cells of MoS_2. Promoted structures were obtained by replacing Mo with Co or Ni at the relevant edge positions. In the case of Co, all Mo atoms at the $(\bar{1}010)$ edge were replaced by Co, which is known to be the most energetically favorable location of Co [34,38,56]. In the case of Ni, locations at both edges were considered and either 50 or 100% of the Mo atoms at the edge were replaced by Ni. Hydrogen adsorption was also investigated, but based on the adsorption energies found, the concentration of adsorbed hydrogen was estimated to be negligible under experimental conditions for all Co–Mo–S and Ni–Mo–S edges investigated. The plane wave DFT code DACAPO [57,58] was used for all calculations. The Brillouin zone was sampled by Monkhorst–Pack sampling [59] using 12 k-points in the x-direction and 1 k-points in the y- and z-directions for the 1×6 stripe and 6 k-points in the x-direction and 1 k-points in the y- and z-directions for the 2×6 unit-cell. A plane wave cutoff of 30 Rydberg and a density cutoff of 60 Rydberg were used for the Co–Mo–S calculations, and a plane wave cutoff of 25 Rydberg and a density cutoff of 50 Rydberg were used for the Ni–Mo–S calculations. This double-grid technique [60] ensured sufficient accuracy of energies and forces. Ultrasoft pseudopotentials were used for all species except sulfur, for which a soft pseudopotential was used when investigating Co–Mo–S [61,62]. Ultrasoft pseudopotentials were used for all species when investigating Ni–Mo–S, allowing for the lower plane wave cutoff. Fermi smearing with an electronic temperature of $k_B T = 0.1$ eV/Å was used for all calculations. The PW91 functional [63] was used as an exchange-correlation functional. Co and Ni are both magnetic materials; thus, all calculations were performed spin-polarized. All structures were relaxed until the remaining total force was below 0.1 eV/Å. We carefully checked that our results were well converged with these parameters.

Relative edge free energies for the promoted edges (γ) were used to evaluate the edge stability at experimental conditions and were calculated using the DFT energies and the thermodynamic model introduced by [38,54,64,65] by considering the chemical potentials of sulfur (μ_S) and hydrogen (μ_H) [41,54]. As described in detail in Refs. [41,54], it was necessary to consider chemical potential parameters for both synthesis conditions (sulfiding: $\mu_S = -0.39$ eV, $\mu_H = -1.08$ eV) and vacuum conditions (imaging: $\mu_S = -0.29$ eV, $\mu_H = -0.49$ eV) due to the quench-and-look approach in the experiments. For the STM analysis in this paper, simulated STM images were calculated using the Tersoff–Hamann model [66]. The STM simulations were performed as reported in [54] by matching the corrugation on the MoS_2 basal plane to the experimentally measured value of 0.2 Å and then plotting calculated contours of constant local density of the electron states. For some simulations, the effect of the Au substrate also was included, but generally this did not change the qualitative appearance of the edges [55].

3. Results and discussion

The synthesis procedure for the promoted hydrotreating model catalyst produces two significantly different types of surface structures: (i) cobalt- or nickel-sulfide islands at the Au(111) step edges, and (ii) well-dispersed Co–Mo–S or Ni–Mo–S nanoclusters on the terraces of the Au(111) substrate. The growth of cobalt or nickel-sulfide islands at the substrate step edges (Figs. 2a and 2b) arises due to the excess amounts of Ni or Co added relative to the available number of substitutional sites on the MoS_2 nanoclusters. The tendency to form

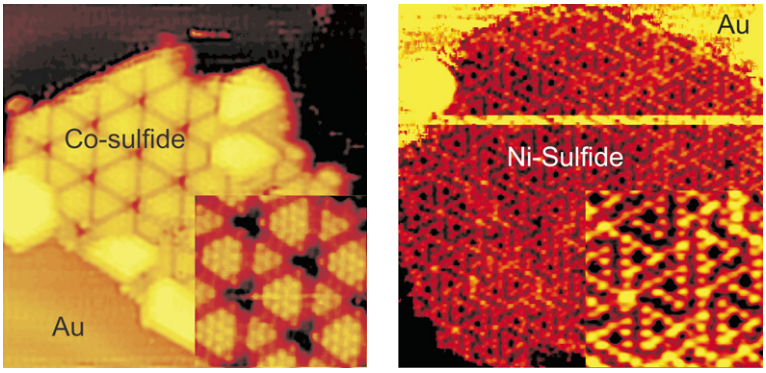

(a) (b)

Fig. 2. (a) Cobalt sulfide formed on Au(111). The insert shows the proposed $Co_3S_4(111)$ facet. Adapted from [39]. (b) Nickel sulfides formed at the step edges of the Au(111) surface. The insert shows the proposed $Ni_3S_2(111)$ facet.

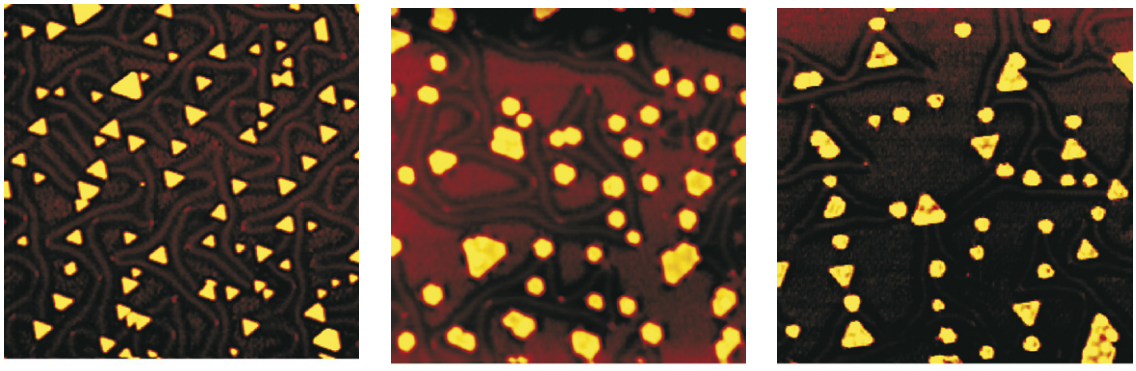

(a) (b) (c)

Fig. 3. (a) Morphology of unpromoted, Co-promoted and Ni-promoted nanoclusters. (a) MoS_2 on Au(111) (700 × 700 Å^2). (b) Co–Mo–S on Au(111) and 700 × 700 Å^2. (c) Ni–Mo–S on Au(111) 700 × 700 Å^2.

these sulfides at the step edges is initiated by a high mobility of Co and Ni on the Au(111) surface in the presence of H_2S. The structures observed with STM match the (111) facets of Co_3S_4 and Ni_3S_2, respectively, but considering the fact that such sulfides do not have an appreciable HDS reactivity [5], the following discussion concentrates on the much more interesting crystalline Co–Mo–S and Ni–Mo–S nanoclusters nucleated on the Au(111) terraces.

The main indicator for the formation of promoted Co–Mo–S and Ni–Mo–S phases is a pronounced change in the equilibrium morphology relative to that of unpromoted MoS_2 nanoclusters. The large-scale STM images in Fig. 3 clearly illustrate this change in morphology. The unpromoted MoS_2 nanoclusters (Fig. 3a) are mainly triangular while the Co–Mo–S (Fig. 3b) and Ni–Mo–S (Fig. 3c) exhibit truncated morphologies. The unpromoted triangular MoS_2 nanoclusters shown in Fig. 3a have previously been characterized in detail [40–42,67], and they are characterized as single-layer MoS_2 nanoclusters oriented with the $MoS_2(0001)$ facet in parallel to the substrate. The changes observed in the morphology of the promoted clusters relative to the triangular MoS_2 nanoclusters formed under the same conditions were invoked only by the presence of promoter atoms (with all other synthesis parameters the same); thus, the observed shift in morphology can be attributed directly to the incorporation of promoters into the MoS_2 structure, that is, the formation of Ni–Mo–S or Co–Mo–S structures.

Atomically resolved STM images of Co–Mo–S and Ni–Mo–S nanoclusters also revealed a flat and perfectly crystalline basal plane consisting of hexagonally arranged protrusions with an interatomic spacing of 3.16 Å (Figs. 4a and 7a). The height profile of the clusters corresponded to the values found for the single-layer MoS_2 nanoclusters in previous studies [40]; thus, the addition of the promoters left the internal structure of the cluster unchanged as MoS_2. Therefore, the truncated morphology of the promoted clusters may be explained by a perturbation of the edge free energy of the two low-index edge terminations of MoS_2 driven by the affinity of Co or Ni to replace Mo at the edges.

3.1. Co–Mo–S morphology

The near-hexagonal shape observed for Co–Mo–S implies that two types of low-indexed edge terminations are exposed in the clusters (see Fig. 4a). The exact shape is according to the Wulff-theorem determined by the competition between two low-index MoS_2 edges, referred to as the $(\bar{1}010)$ edge (S edge) and $(10\bar{1}0)$ edge (Mo edge), as illustrated in Fig. 1b for a hypothetical, single-layer MoS_2 nanocluster [5,40,64,68]. The triangular shape observed previously for unpromoted MoS_2

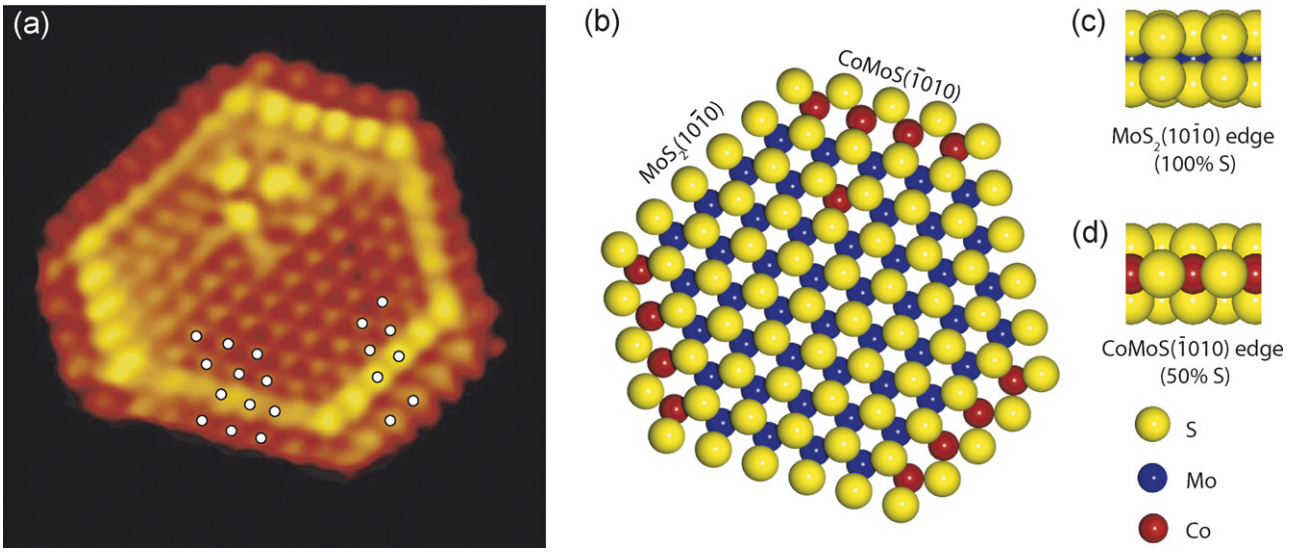

Fig. 4. (a) Atom-resolved STM image of Co–Mo–S (51 × 52 Å^2, $V_t = 95.2$ mV, $I_t = 0.81$ nA). (b) Ball model of the Co–Mo–S. (c) Side view of the $MoS_2(10\bar{1}0)$ edge. (d) Side view of Co-substituted Co–Mo–S($\bar{1}010$) edge. S: yellow, Mo: blue, Co: red.

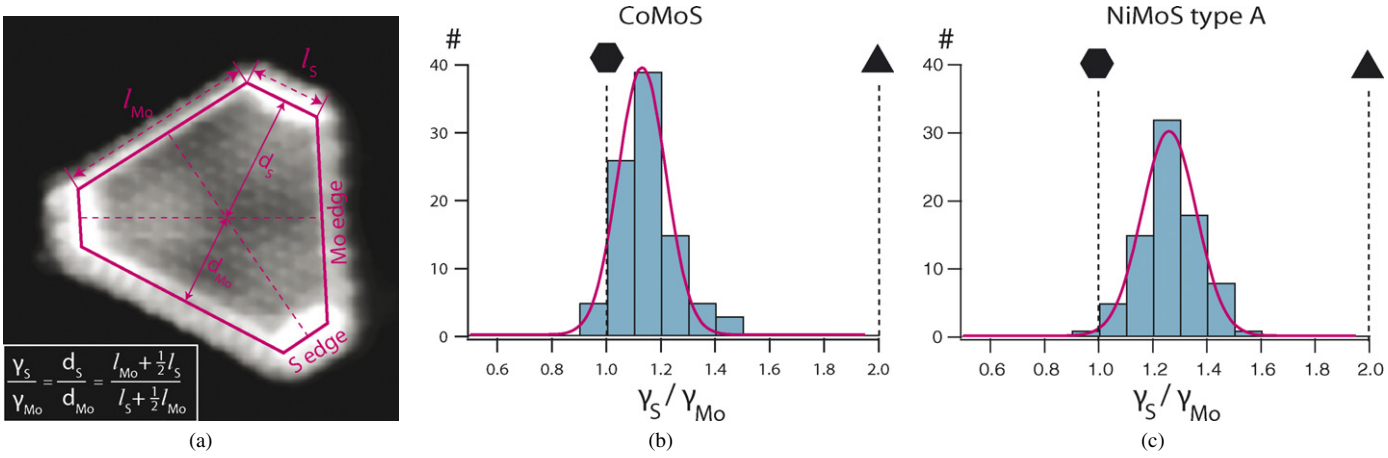

Fig. 5. (a) Ratio of edge free energies ($\gamma_{(\bar{1}010)}/\gamma_{(10\bar{1}0)}$) is connected to the cluster shape. (b) Histogram of relative edge free energies for Co–Mo–S particles, and (c) for Ni–Mo–S.

(Fig. 3a) reflected that the ratio of the edge free energies of these edges was greater than a factor of two ($\gamma_{(\bar{1}010)} > 2\gamma_{(10\bar{1}0)}$); that is, only ($10\bar{1}0$) edges (Mo edges) we exposed. The situation is clearly changed for Co–Mo–S and as was shown in Ref. [39], it is possible in atom-resolved STM images to identify both the ($\bar{1}010$) edge and ($10\bar{1}0$) edge in the Co–Mo–S particles. In the present study, measuring the distribution of both edges for a large number of clusters provides an estimate of the ratio between the edge free energies in Co–Mo–S $\gamma_{(\bar{1}010)}/\gamma_{(10\bar{1}0)}$ to be 1.1 ± 0.2; that is, the ($10\bar{1}0$) edge is only slightly more stable in Co–Mo–S (see Figs. 5a and 5b).

3.2. Co–Mo–S edge structure

On the basis of the detailed atomic-scale information provided by the STM images (Fig. 4), a structural model of the Co–Mo–S nanoclusters was proposed in Ref. [39] in which the Co–Mo–S clusters are terminated by ($10\bar{1}0$) edges with no Mo atoms substituted by Co and ($\bar{1}010$) edges in which all Mo atoms are substituted by Co atoms. The unpromoted ($10\bar{1}0$) edge type in Co–Mo–S, shown in Fig. 4a, is characterized by a row of edge protrusions located with the regular 3.16 Å interatomic distance of MoS_2, but with the edge protrusions clearly located *out* of registry with the lattice of S atoms belonging to the basal plane. This edge also is identified by the presence of a bright brim (0.4 ± 0.1 Å) located adjacent to the outermost edge protrusions. This appearance is in exact qualitative and quantitative agreement with the ($10\bar{1}0$) edge structure observed for unpromoted MoS_2 triangles [40,41,55].

The morphological change observed with STM for the promoted system is thus induced by the tendency for Co to be located *only* at the Co–Mo–S($\bar{1}010$) edges. As depicted in the ball model in Figs. 4b and 4d, the Co–Mo–S($\bar{1}010$) edges are proposed to have a *tetrahedral* coordination of the Co atoms if the outermost sulfurs are bridge-bonded S monomers. The edge stabilities obtained from DFT calculations in Fig. 6a confirm this configuration, as well as a configuration with 75% sul-

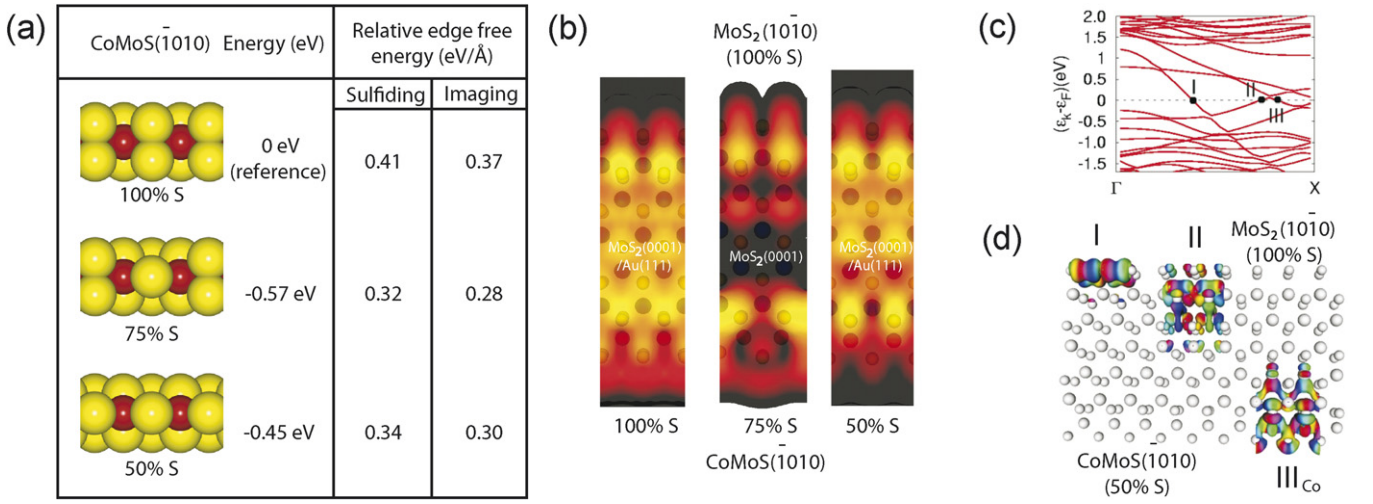

Fig. 6. (a) DFT results for Co–Mo–S($\bar{1}010$) edges (S: yellow, Co: red), (2×6 unit cell). (b) STM simulation (1×6 unit cell) of the Co–Mo–S($\bar{1}010$) edge with 100, 75, and 50% sulfur. (c) Band structure of the MoS_2 slab exposing the 50% S Co–Mo–S($\bar{1}010$) and $MoS_2(10\bar{1}0)$. (d) Plot of the wavefunction contours associated with the three metallic edge states in Co–Mo–S.

fur as the most stable structures differing by only 0.02 eV/Å in edge free energy. Edge terminations with sulfur coverage <50% are not considered further, because such configurations were found to be very unstable [36,38,56]. The possibility that Co substitutes only a fraction of the Mo atoms at the Co–Mo–S($\bar{1}010$) edges can also be ruled out, because this would not give rise to the observed regular edge pattern in STM images. A detailed comparison of the experimental image with a simulated edge reveals the structure of the observed Co–Mo–S edge. A grid superimposed on the basal plane S atoms near the Co–Mo–S($\bar{1}010$) edges in the experimental image (Fig. 4a) shows edge protrusions located at positions *in* registry with the basal plane S lattice. Compared with the position of the bulk lattice, however, a slight displacement of ∼0.5 Å perpendicular away from the edge can be seen. The ($\bar{1}010$) edge also exhibits a very bright brim parallel to the edge in the row immediately behind the edge protrusions. The brim structure is significantly brighter than that of the ($10\bar{1}0$) edge, with a height of 0.9 ± 0.2 Å above the basal plane atoms.

Agreement with this appearance in the STM image was obtained only for the simulation of the Co–Mo–S($\bar{1}010$) edge with a 50% S coverage (Fig. 6b). This assignment of the structure of the Co-promoted edge is in good accordance with previous STM simulations by Schweiger et al., who also used a calculation of a cluster structure to directly calculate the relative stability of the two edge types in Co–Mo–S as a function of μ_S [38]. The predicted truncated hexagonal shape was also in agreement with the experiment in Ref. [39].

The STM simulation for the Co–Mo–S($\bar{1}010$) edge shows that protrusions at the edges reflect the position of the monomer S atoms, and that a bright brim is present at the position of the adjacent row of sulfur atoms. These sulfurs are also coordinated to the substituted Co atoms. As in the experimental image, the brim in the simulated image (Fig. 6b) also shows a significant corrugation in cross-sections drawn parallel to the edge. It is important to emphasize that the bright brim in Co–Mo–S does not reflect S atoms located geometrically higher than the basal plane. Our STM simulations and that in Ref. [38] performed without the gold substrate also show that this qualitative appearance is not influenced by the gold substrate. As for the $MoS_2(10\bar{1}0)$ edges [54,55], the brim is related instead to a perturbation of the electronic structure at the edges of the clusters and the existence of metallic, one-dimensional edge states. The edge states in Co–Mo–S are revealed in the electronic band structure of the Co-substituted ($\bar{1}010$) edge in Fig. 6c. The band structure diagram shows three bands (denoted I, II, and III_{Co}) penetrating into the band gap region of MoS_2 and crossing the Fermi level. Edge states I and II pertain to the $MoS_2(10\bar{1}0)$ edge and are the same as those reported previously in [55]. In the plot of the wave-function contours in Fig. 6d, the edge state III_{Co} is located directly at the Co-substituted Co–Mo–S($\bar{1}010$) edge. The edge state is localized on the outermost four rows of atoms counted inward from the edge and is responsible for the very intense bright brim. The resemblance of the brim associated with the metallic edge state III_{Co} pertaining to the promoted edge with that of the unpromoted MoS_2 nanoclusters is very interesting from a catalytic standpoint, because the metallic brim sites on the $MoS_2(10\bar{1}0)$ edges are relatively strong adsorption sites active in HYD and the C–S splitting of thiophene molecules [42,46]. In particular, it is speculated that the close vicinity of the metallic brim sites and edge sites on the Co–Mo–S($\bar{1}010$), which contains intrinsically undercoordinated Co atoms, may provide a favorable environment for reaction.

3.3. Ni–Mo–S morphology

A distinct change of the particle morphology of Ni–Mo–S is also observed relative to that of the unpromoted MoS_2 nanoclusters (Figs. 3a and 3c). However, in contrast to the Co-promoted case, two types of Ni–Mo–S clusters are seen. These clusters are distinguished in terms of the size and shape and may coexist on the same sample. The first type (Fig. 7) is characterized by a truncated triangular shape similar to that of the Co–Mo–S nanoclusters. The second (Fig. 8) shows a more com-

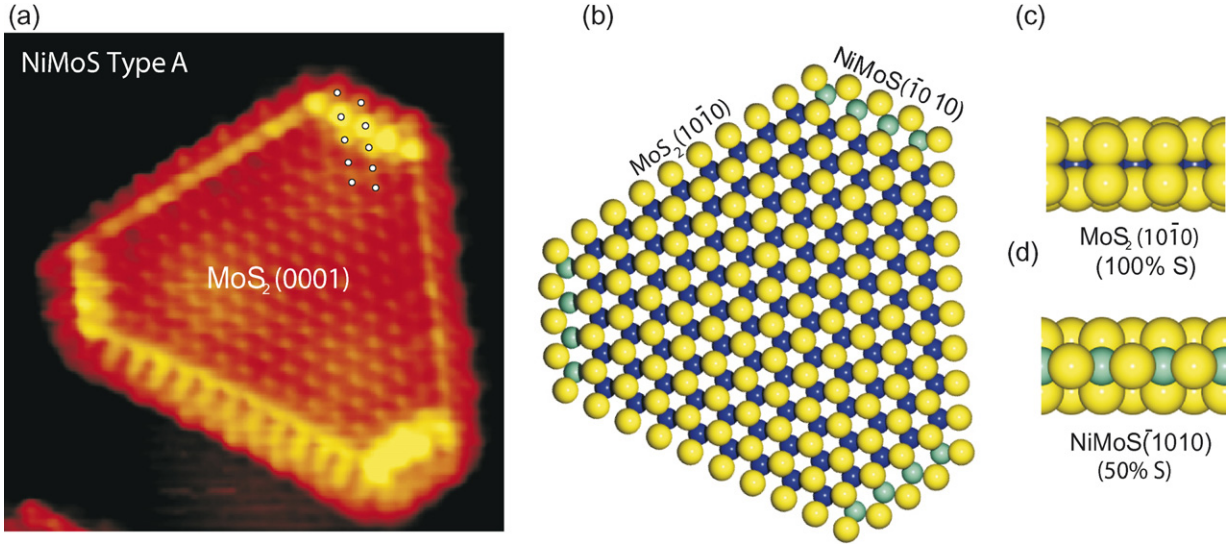

Fig. 7. (a) Atom-resolved STM image of type A Ni–Mo–S (61 × 61 Å^2, $V_t = -600$ mV, $I_t = -0.51$ nA). (b) Ball model of type A Ni–Mo–S. (c) Side view of the $MoS_2(10\bar{1}0)$ edge. (d) Side view of the Ni–Mo–S($\bar{1}010$) edge. S: yellow, Mo: blue, Ni: cyan.

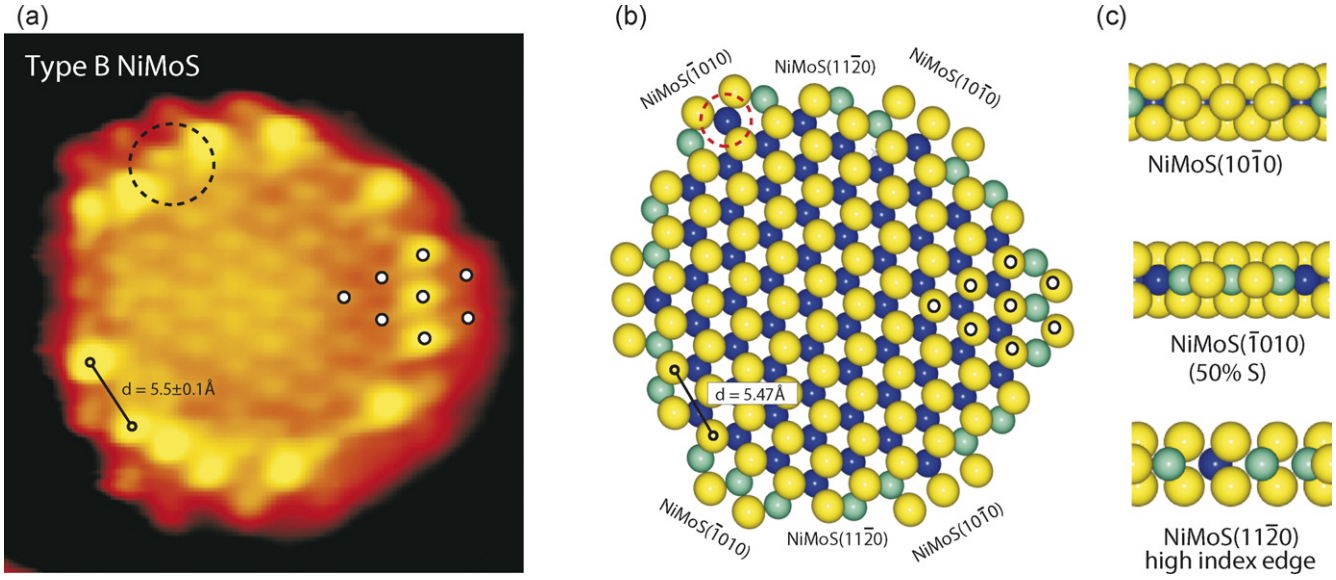

Fig. 8. (a) Atom-resolved STM image of type B Ni–Mo–S (39 × 40 Å^2, $V_t = -520$ mV, $I_t = 0.44$ nA). (b) Ball model of type B Ni–Mo–S. (c) Side views of Ni–Mo–S($\bar{1}010$), Ni–Mo–S($10\bar{1}0$) and Ni–Mo–S($11\bar{2}0$) edges. S: yellow, Mo: blue, Ni: cyan.

plex morphology that fits a dodecagonal shape. In what follows, the truncated triangular structures are referred to as *type A Ni–Mo–S*, and the dodecagonal-like nanoclusters are termed *type B Ni–Mo–S*.

The distribution of type A and type B Ni–Mo–S nanoclusters is very sensitive to the annealing temperature of the preparation. The particle size distribution shown in Fig. 9 illustrates this effect for three synthesis temperatures in the range 673–773 K. At the normal synthesis temperature of 673 K, the size distribution exhibits a quite typical distribution due to nucleation and growth on a uniform substrate. The average size of the nanoclusters is ∼800 Å^2, and a small shoulder is found at higher values. As the temperature is increased, the distribution shifts to a clear bimodal distribution, with a peak remaining close to the original size of ∼800 Å^2 and a much broader peak at higher average size that increases in intensity and shifts to higher values as a function of temperature. The gradual redistribution of the average cluster size is attributed to a higher surface mobility during synthesis at increased temperatures. The correlation between the cluster shape and size indicates that the peak fixed at ∼800 Å^2 is associated exclusively with the dodecagonally shaped *type B Ni–Mo–S*, whereas the larger clusters exclusively adopt the shape corresponding to the truncated triangular *type A Ni–Mo–S*. After prolonged sulfidation (up to 1 h), the unexpected bimodal distribution remained the same, indicating that the observations are not the result of kinetic limitations during growth. Interestingly, these observations indicate that the equilibrium shape of Ni–Mo–S (i.e. the ratio of edge free energies) depends on the size of the particles. A surprising variation in edge structure and sulfur coverage as a function of nanoclus-

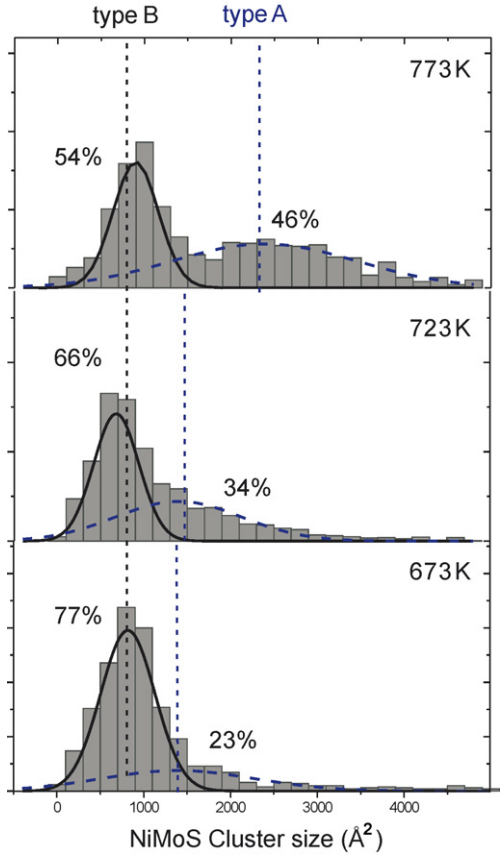

Fig. 9. Particle size distribution for Ni–Mo–S prepared at three temperatures from 673 to 773 K. Bin size is 200 Å^2. For clarity, the distribution is fitted with Gaussians assuming a bimodal distribution.

ter size also was recently observed for the unpromoted MoS_2 triangles formed under similar sulfiding conditions [67].

3.4. Type A Ni–Mo–S edge structure

Fig. 7 shows an atomically resolved STM image of a type A Ni–Mo–S particle. The hexagonal morphology observed with STM directly implies that both low-index edge terminations of MoS_2 are exposed in the nickel promoted clusters, i.e. a $(\bar{1}010)$ edge and a $(10\bar{1}0)$ edge. The longer edges of the Ni–Mo–S nanocluster in Fig. 7 are observed to be identical to the fully sulfided $MoS_2(10\bar{1}0)$ edges (100% S) observed on unpromoted MoS_2 triangles. Thus, for the larger type A Ni–Mo–S, the substitution of Ni promoter atoms appears to be disfavored at the $(10\bar{1}0)$ edges under the conditions of the experiment. As shown in Fig. 5c, the ratio between the edge free energies of the Ni substituted Ni–Mo–S$(\bar{1}010)$ edge and the unsubstituted $(10\bar{1}0)$ edge is found to be $\gamma_{(\bar{1}010)}/\gamma_{(10\bar{1}0)} = 1.3$ for the type A Ni–Mo–S; that is, the relative stability is slightly in favor of the unpromoted $(10\bar{1}0)$ edge.

In Fig. 7, the Ni–Mo–S$(\bar{1}010)$ edges in the Ni–Mo–S nanocluster are again observed to contain a very intense brim in the second row behind the edge. A line scan reveals the height of the brim in Ni–Mo–S to be 0.8 ± 0.1 Å, slightly lower than that of the corresponding Co–Mo–S$(\bar{1}010)$ edges. Furthermore, the edge protrusions themselves are observed to be placed *in* registry with the basal plane atoms, and the outermost protrusions are shifted slightly (∼0.8 Å) away from the edge. Edges with alternating Mo and Ni atoms located on the $(\bar{1}010)$ edge have been proposed to be energetically feasible [36], but the present experiments demonstrate no tendency to form edges with a partial Ni-substitution in the type A Ni–Mo–S nanoclusters, which would give rise to patterns in STM linescans with a periodicity larger than the observed single atomic distance. (The situation may be different for type B Ni–Mo–S, as discussed below.) Therefore, we associate the Ni–Mo–S$(\bar{1}010)$ edges in Fig. 7 with a structure in which Ni atoms have completely replaced every Mo atom at the edge positions.

Numerous edge configurations of Ni–Mo–S$(\bar{1}010)$ are possible, and due to the comparatively small differences in energy, we have investigated many of them in detail, simulating the corresponding STM images (Fig. 10b and Supplementary material). The most significantly reduced configurations (0 and 25% sulfur coverage) are found to be energetically unstable and thus not presented here. We also do not see evidence of partially Ni-substituted $(\bar{1}010)$ edges. The three most stable configurations corresponding to 50, 75, and 100% sulfur coverage are shown in Fig. 10a. A fully sulfided Ni–Mo–S$(\bar{1}010)$ edge is the most stable structure in terms of edge free energies, with the 75 and 50% S coverages being about 0.03 eV/Å less stable. Only the simulation of the 50% sulfur coverage is, however, found to match the experimental images of the Ni–Mo–S$(\bar{1}010)$ (Fig. 10b and Supplementary material). This difference may be due to a corner effect that dominates for the rather short cluster edges of an effect of the substrate, which is not accounted for in the DFT calculations. The relative edge free energies for the 50, 75, and 100% S coverage are the same within 0.03 eV/Å, and, given, the short edges (10–20 Å), a small offset in energy due to a corner effect might change the stability. The Ni–Mo–S$(\bar{1}010)$ edge terminations have been investigated by Schweiger et al. [38], who also calculated the equilibrium shape. A similar apparent offset in the energies seems to be present in these studies because the observed 50% S coverage and ratio of edge free energies if Ni–Mo–S type A $(\gamma_{(\bar{1}010)}/\gamma_{(10\bar{1}0)} = 1.3)$ is predicted only at a significantly lower chemical potential of sulfur than used in the experiment.

The STM simulation given in Fig. 10b shows the unpromoted $MoS_2(10\bar{1}0)$ edge with dimers (upper part) appearing as in previous studies [40,55]. For the Ni–Mo–S$(\bar{1}010)$ edge, the best match is clearly seen for the 50% S coverage, where the protrusions on the Ni–Mo–S$(\bar{1}010)$ edge (lower part) reflect sulfur monomers, and, as observed in the experiment, a very bright brim is located on the sulfurs in the second row behind the edge. Again, the bright brim of the Ni–Mo–S$(\bar{1}010)$ edge can be related to edge states that render the Ni-substituted edge metallic. In the band structure for this edge configuration (Fig. 10c), four bands are seen to cross the Fermi level. From the plot of the wavefunction contours, edge states I and II are found to belong to the $MoS_2(10\bar{1}0)$ edge, whereas edge states III_{Ni} and IV_{Ni} are located at the Ni-substituted Ni–Mo–S$(\bar{1}010)$ edge. Edge state III_{Ni} is similar to edge state III_{Co} of the Co–Mo–S$(\bar{1}010)$ (Fig. 6d) and is the state giving rise to the bright brim. Nonetheless, it is interesting that the edge state IV_{Ni} has

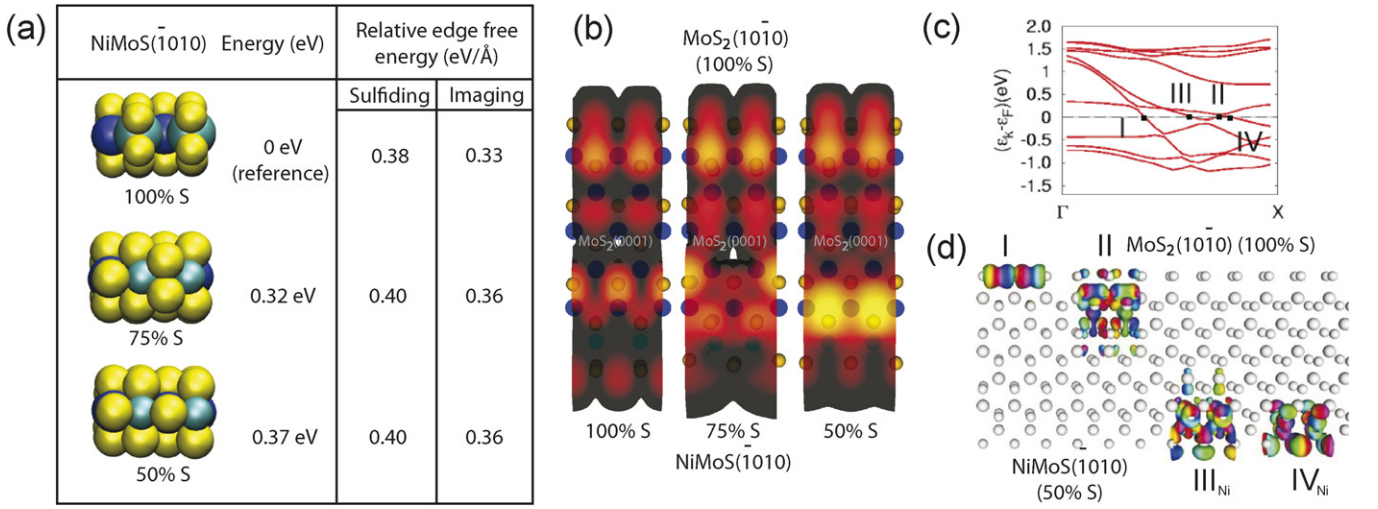

Fig. 10. (a) DFT results for the (100% Ni) Ni–Mo–S($\bar{1}010$) edge (2×6 unit cell). (b) STM simulation (1×6 unit cell) of the fully Ni-substituted Ni–Mo–S($\bar{1}010$) edge with a 50, 75, and 100% S coverage. (c) Band structure, and (d) plot of wavefunction contours associated with the two metallic edge states in 50% S Ni–Mo–S($\bar{1}010$).

no Co–Mo–S counterpart. This edge state has a p_z-like geometry on the front S atoms. The possibilities that this edge state plays a role in catalysis and that the different activity and selectivity of Ni–Mo–S compared with Co–Mo–S is related to this additional metallic edge state in Ni–Mo–S should be investigated.

In conclusion, it was found that the truncated hexagonal type A Ni–Mo–S clusters are terminated by unpromoted, fully sulfided $MoS_2(10\bar{1}0)$ edges and fully Ni-substituted Ni–Mo–S($\bar{1}010$) edges with 50% coverage of sulfur.

3.5. Type B Ni–Mo–S edge structure

The smaller type B Ni–Mo–S clusters (Fig. 8) are characterized by a markedly different cluster shape than type A Ni–Mo–S (Fig. 7). The shape of type B Ni–Mo–S particles can be described as dodecagonal, that is, particles exposing 12 edges. Thus, the shape of type B Ni–Mo–S particles cannot be described as originating from a simple low-index edge-truncated shape of a triangle as in the Wulff-type model in Fig. 1b. Instead, a model that includes edges with higher Miller indices must be included. As shown in Fig. 8, a model in which a MoS_2 hexagon exposing Ni–Mo–S($10\bar{1}0$)-type edges and Ni–Mo–S($\bar{1}010$)-type edges is truncated at the corners by 6 new edges of the ($11\bar{2}0$)-type matches the experiment closely. Thus, in the smaller type B Ni–Mo–S, the Ni not only seems to affect the S edges, but also appears to stabilize edges of the ($11\bar{2}0$) type.

A ball model of a type B Ni–Mo–S cluster is illustrated in Fig. 8b. Note that the cluster in the experimental image (Fig. 8a) contains only 11 edges; that is, only five of six possible corners have been truncated by Ni to form Ni–Mo–S($11\bar{2}0$) edges. The Ni-substituted Ni–Mo–S($\bar{1}010$) edges are readily identified in the atom-resolved image in Fig. 8 because they are imaged in the same way as the Ni–Mo–S($\bar{1}010$) edges in the larger type A Ni–Mo–S particles (Fig. 7). Also note that one of the Ni–Mo–S ($\bar{1}010$) edges in Fig. 8 exhibits a pattern most likely resulting from partial substitution of Mo with Ni (indicated by a black dashed circle), but this is observed only rarely and thus should be considered more a single defect than a stable structure.

The ($10\bar{1}0$) edges are rotated 60 degrees relative to the ($\bar{1}010$) edges in the dodecagonal type B Ni–Mo–S particles. A zoom-in on a ($10\bar{1}0$) edge of a type B Ni–Mo–S cluster is shown in Fig. 11a. The type B Ni–Mo–S($10\bar{1}0$) edge seems different from the type A Ni–Mo–S($10\bar{1}0$) edges found in the larger particles (Fig. 7). First, the brim in the middle part of the edge is reduced almost to the level of the basal plane, whereas it has a much higher intensity near the corners. We associate this appearance with substitution of some of the Mo atoms by Ni atoms at the two edge positions near the corners between a Ni–Mo–S($\bar{1}010$) edge and a ($11\bar{2}0$) high-index edge. This is shown in detail in the ball model in Fig. 11b. Note that Ni was added in excess amounts, and thus the observed partially substituted Ni–Mo–S($10\bar{1}0$) can be considered an intrinsic and stable feature of the Ni–Mo–S type B particles.

In the STM image in Fig. 11a, the outermost edge region of the type B Ni–Mo–S($10\bar{1}0$) edges has a very low intensity. This observation may indicate that sulfur atoms are missing on the ($10\bar{1}0$) edges compared with the fully sulfided edges observed in type A Ni–Mo–S, Co–Mo–S, and MoS_2. To understand the observed structure for type B Ni–Mo–S, further DFT calculations were performed for the ($10\bar{1}0$) edges. For the theoretical analysis, models of the ($10\bar{1}0$) edges in which Mo edge atoms are either fully substituted by Ni atoms or partially substituted with alternating Ni on every second site are considered. These configurations represent parts of the ($10\bar{1}0$) edges terminated with either Ni–Ni or Ni–Mo sections, respectively. The relative edge free energies in Figs. 11c and 11e are calculated with the same reference and thus are directly comparable. The fully Ni-substituted Ni–Mo–S($10\bar{1}0$) with 0% sulfur is seen to be most stable. But again, the edge free energy differences relative to the most stable partially substituted edges are of the order of 0.04 eV/Å; thus, for short edges (~10 Å), as in type B Ni–Mo–S, partial substitution cannot safely be neglected. The

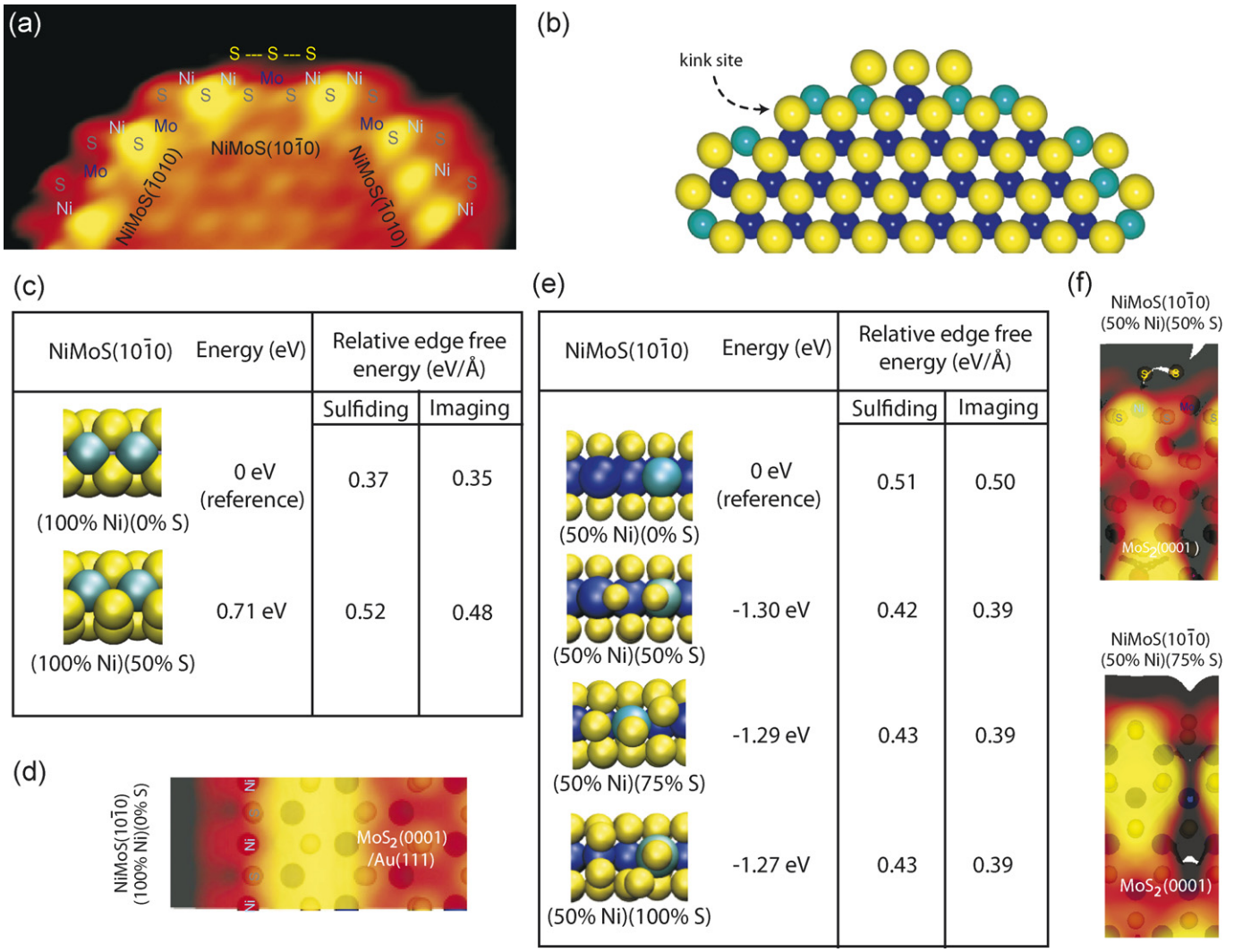

Fig. 11. (a) Zoom-in on a type B Ni–Mo–S nanocluster. (b) A topview ball model. (c) DFT results (2×6 unit cell) for a fully substituted (100% Ni) Ni–Mo–S(10$\bar{1}$0) edge. (d) STM simulation of 100% Ni and 0% S Ni–Mo–S(10$\bar{1}$0) edge. (e) DFT results (2 × 6 unit cell) for a 50% Ni Ni–Mo–S(10$\bar{1}$0) edge. (f) STM simulation of (50% Ni) Ni–Mo–S(10$\bar{1}$0) edge with 50% S and 75% S.

fully Ni-substituted edge with 0% sulfur coverage represents the parts of the ($\bar{1}$010) edge with neighboring Ni–Ni pairs near the corners as shown in (Fig. 11b). The simulation (Fig. 11d) produces a bright region behind the Ni row, as seen in the experiment. These brim regions have a comparable height to the brim on the Ni-substituted ($\bar{1}$010) edge, as also seen in the experiment; moreover, the outermost edge region in which no S atoms are present indeed has a very low intensity. Due to the higher affinity of Mo to sulfur, the situation is likely different in the middle part of the edge, where both Ni and Mo are present at neighboring sites on the edge. Fig. 11e shows the three sulfur coverages in the range 50–100% found to be most likely edge terminations for an edge exposing alternating Ni or Mo atoms (50% Ni substitution). All three investigated sulfur coverages in the range 50–100% are very close in terms of edge free energy (<0.01 eV/Å); however, the STM simulations of the edge with 75% (Fig. 11f, lower part) or 100% sulfur show no clear match with the experimental image. Instead, the 50% S-covered edge (Fig. 11f, upper part) reproduces the experimental STM image, including the bright protrusion behind the Ni site and a depleted intensity behind the Mo site. Furthermore, it is seen that both S atoms adsorbed on Ni or Mo are associated with a very low intensity, as also observed in the experiment. Note that previous DFT studies also found a very small energy difference between an unpromoted and a Ni-substituted (10$\bar{1}$0) edge [38]; a competition between the two promoted and unpromoted edges depending on the experimental conditions was proposed.

Our STM findings clearly reveal that both configurations may coexist on the same edge. This finding implies that the tendency for Ni substitution is linked to the overall cluster size and appears to be predominant only at positions adjacent to a (11$\bar{2}$0) edges of the octahedral Ni–Mo–S type B particles.

The short edges on either side of the Ni–Mo–S(10$\bar{1}$0) edge in Fig. 11a appear to be based on the (11$\bar{2}$0) edge structure. They are identified by their orientation ±30 degrees relative to the (10$\bar{1}$0) and ($\bar{1}$010) edges and also by the two bright protrusions (see Fig. 8a) separated by ∼5.5 Å, which precisely matches the interatomic periodicity of 5.47 Å in the direction parallel

to the $(11\bar{2}0)$ edges of MoS_2 (Fig. 8b). The observation of these edges in equilibrium structures is highly interesting, because such high-index-edge terminations were once considered too energetically unfavorable. The Ni is structurally similar to the Ni on the Ni–Mo–S$(10\bar{1}0)$ edge but has a lower sulfur coordination, because only S monomers are present on the neighboring Ni–Mo–S$(\bar{1}010)$ edge. The more open structure of the corner site may provide an attractive site for hosting reactive sulfur vacancies during reaction conditions, and clearly an improved understanding of the catalytic relevance of such sites in future DFT and STM investigations is important. Typically the $(11\bar{2}0)$ edges are very short, spanning only a single unit cell, and thus could be considered a corner effect for the finite-size clusters; surprisingly, however, we even observed clusters with $(11\bar{2}0)$ edges two or three unit cells wide. The abundance of these edge terminations suggests that the $(11\bar{2}0)$ cluster termination must have comparable edge free energy to the more closely packed $(10\bar{1}0)$ and $(\bar{1}010)$ edges for this cluster size.

Cluster DFT calculations of Ni–Mo–S particles of different sizes could shed more light on the observed size-dependent affinity for Ni substitution and Ni–Mo–S morphology. They also could help determine whether the $(11\bar{2}0)$ edges should be considered a stable edge termination of Ni–Mo–S or a corner effect that dominates only for the smallest Ni–Mo–S clusters.

4. Comparison of Co–Mo–S and Ni–Mo–S structures with X-ray absorption results

It is interesting to compare the present surface science results with previous X-ray absorption fine-structure (XAFS) studies that have provided information on the average interatomic distances and coordination numbers of Co and Ni promoter atoms for supported Co–Mo–S and Ni–Mo–S particles. To avoid the influence from promoter atoms in structures other than Co(Ni)–Mo–S (in, e.g., the alumina support), the structure surrounding the Co and Ni atoms was typically studied on carbon-supported catalysts. For Co–Mo–S, the structural surroundings of the Co present in carbon-supported Co–Mo sulfide catalysts was studied by X-ray absorption near-edge structure (XANES) spectroscopy at the Co K-edge. Comparing XANES spectra of the catalysts with those of Co_9S_8 and CoS_2 model compounds shows [30,69,70] that the Co atoms in the Co–Mo–S state have a distorted 5- to 6-fold S coordination and that on average, every Co atom is in contact with 2 Mo atoms at a distance of 2.80 Å [30]. Comparing the XANES structure of carbon-supported sulfided Ni–Mo catalysts with well-defined model structures [29,31,71] demonstrates that the Ni atoms have a sulfur coordination number below 6, different from that of an octahedral-like S coordination. The Ni atom in Ni–Mo–S have been suggested to be located in a square pyramid of 5 S atoms at a distance of about 2.21 Å from the S atoms. An EXAFS contribution due to a Mo atom at 2.82 Å from the Ni atom also has been identified [72].

Tables 1 and 2 summarize main XAFS results in the literature for the coordination number and interatomic distances of Co–S, Co–Co, Ni–S, and Ni–Ni obtained from studies of Co–Mo and Ni–Mo sulfided catalysts ([14,69,73–75] and [29,31,71,72]). These tables also present the corresponding interatomic distances and coordination numbers taken from the detailed models of the promoted edges in Co–Mo–S and Ni–Mo–S in the STM experiments and DFT calculations. To allow direct comparison with the XANES values, the STM/DFT values from this study are calculated from the weighted average coordination of all Co or Ni atoms in the Co–Mo–S and type A and B Ni–Mo–S models proposed earlier (Figs. 4, 7, and 8). The average coordination values of the promoters are functions of cluster size and shape (degree of truncation), because corner or edge promoter atoms have a different coordination. This is a particularly important effect for small cluster sizes. There is a general trend toward increasing sulfur coordination when corner sites start to dominate and the promoter-promoter coordination decreases toward 1. The STM experiments typically revealed promoted edges 2 to 6 unit cells wide for both Ni- and Co-promoted edges; therefore, the data range listed in the tables reflects the actual variation in the size and truncation (Fig. 5) of the observed Co–Mo–S and Ni–Mo–S nanoclusters. The interatomic distances in the STM/DFT row are determined from DFT calculations.

Table 1
Coordination numbers and interatomic distances for Co in Co–Mo–S

	$N_{Co–S}$	$d_{Co–S}$ (Å)	$N_{Co–Co}$	$d_{Co–Co}$ (Å)
Co–Mo–S				
STM/DFT	4.5–5.3	2.10	1.3–1.7	3.22
EXAFS	4.9–5.5	2.20–2.26	0.6–1.2	2.6–2.9

Note. XAFS data are compiled from [14,69,73–75]. Typical uncertainties of the XAFS values are around 20% for nearest neighbors. Interatomic distances (STM/DFT) are based on the calculated structures.

Table 2
Coordination numbers and interatomic distances for Ni in Ni–Mo–S

	$N_{Ni–S}$	$d_{Ni–S}$ (Å)	$N_{Ni–Ni}$	$d_{Ni–Ni}$ (Å)
Type A Ni–Mo–S				
STM/DFT	4.5–5.3	2.14	1.3–1.7	3.22
Type B Ni–Mo–S				
STM/DFT	4.0–4.6	2.14	1.0–1.2	3.21
EXAFS	4.7–5.6	2.12–2.24	1.0	3.21

Note. XAFS data are compiled from [29,31]. Typical uncertainties of the XAFS values are around 20% for nearest neighbors. Interatomic distances (STM/DFT) are based on the calculated structures.

The agreement of the Co–Mo–S XANES data with the present findings is good in terms of both coordination number and interatomic distances. The XAFS measurements in general estimate a slightly higher sulfur coordination to Co ($N_{Co–S} \approx 4.9–5.5 \pm 1$) compared with the STM experiments. In this context, however, it is noteworthy that many of the Co–Mo–S clusters have one or more Co atoms substituted at bulk sites (Fig. 4). The Co atoms are six-fold coordinated to sulfur, and the presence of Co bulk inclusions may shift the average Co–S coordination upward. Furthermore, the Co–Co coordination is slightly lower on the fully substituted Co–Mo–S$(\bar{1}010)$ edges ($N_{Co–Co} = 0.6–1.2 \pm 1$) compared with the average coordination (corner and edge sites) in the STM-based model

($N_{Co–Co} = 1.3–1.7$). This finding may indicate that Co substitution of Co–Mo–S clusters is incomplete, or that the Co–Mo–S clusters in the industrial alumina-supported catalysts are slightly smaller than those reported in this experiment.

Ni–Mo–S also exhibits good agreement between XANES data and the present STM/DFT results. XANES estimates a Ni coordination number to sulfur of $N_{Ni–S} \approx 4.9–5.5 \pm 1$, which is precisely the value found for the type A Ni–Mo–S particles. In the type B Ni–Mo–S, Ni is substituted at three different type of sites with similar or lower sulfur coordination: the Ni–Mo–S($\bar{1}010$) edges, Ni–Mo–S($10\bar{1}0$) edges, and Ni–Mo–S($11\bar{2}0$) edges. This produces a slightly lower average S coordination number compared with that for type A Ni–Mo–S. In the case of Ni–Mo–S, we never observed inclusions on the basal plane indicating the presence of six-fold coordinated Ni. The values found for the Ni–S coordination could thus indicate that predominantly Ni–Mo–S type A particles are present in the technical Ni–Mo sulfided catalysts. However, these values are very sensitive to actual cluster size, and comparing the Ni–Ni coordination number shows that type B Ni–Mo–S also can match the STM experiment for this particular parameter.

These findings demonstrate that the proposed models for Co–Mo–S and Ni–Mo–S are fully consistent with the XAFS data for technical sulfided Co–Mo and Ni–Mo catalysts. Nonetheless, we emphasize that more than one preferential site of Ni was not considered in previous models, and in general it is unclear whether one or more Ni–Mo–S morphologies were present in the previous studies. The fact that the XAFS data were obtained on samples exposed to HDS relevant conditions (H_2/H_2S mixture), whereas the structures analyzed in the present study were formed in a highly sulfiding atmosphere, also should be taken into account. Regardless, there is nothing to indicate a lower sulfided state of Ni–Mo–S or Co–Mo–S in the XAFS experiments compared with the STM experiments, because the sulfur coordination is estimated to be slightly higher.

5. Conclusion

This study used STM studies and DFT calculations to investigate the atomic-scale structure and morphology of individual Co–Mo–S and Ni–Mo–S nanoclusters synthesized on a gold substrate as model systems for Co- and Ni-promoted MoS_2-based hydrotreating catalysts. In accordance with the widely accepted Co–Mo–S model for the promoted hydrotreating catalyst, we found a distinct tendency for Co and Ni to substitute Mo atoms at edge sites of single-layer MoS_2 nanoclusters, which leads to truncation of the cluster morphology relative to unpromoted MoS_2. An analysis of atom-resolved STM images showed that the substitution occurred only at very specific edge sites in Co–Mo–S and Ni–Mo–S, and, interestingly, that Ni–Mo–S may exist in different structural modifications.

In Co–Mo–S, Co substitution induced an almost hexagonal morphology compared with that triangular morphology of unpromoted MoS_2, and atom-resolved STM images showed that this shift in cluster shape seems to be driven by the tendency for Co to be located only at Co–Mo–S($\bar{1}010$) edge sites. The Co–Mo–S($\bar{1}010$) edges had every edge Mo atom substituted with Co and 50% sulfur coverage. Because in this structure, the sulfur atoms do not occupy the regular MoS_2 lattice positions, the Co atoms have a tetrahedral coordination to sulfur. STM images of the Co-promoted edges revealed a very bright brim structure, indicating a modified electronic structure that were related (through DFT calculations) to the presence of a single metallic edge state pertaining to Co–Mo–S.

For Ni–Mo–S, the morphology and affinity for Ni to substitute Mo were found to depend on cluster size. Larger Ni–Mo–S particles (type A Ni–Mo–S) exhibited a truncated triangular shape similar to that observed for Co–Mo–S nanoclusters, whereas the smaller Ni–Mo–S particles (type B Ni–Mo–S) had a dodecagonal shape. The type A Ni–Mo–S structures are terminated by two types of edges. One of these edges is unpromoted and exhibits the same structure as the $MoS_2(10\bar{1}0)$ edges; the other is a Ni–Mo–S($\bar{1}010$) edge, at which Ni has fully substituted all edge Mo sites and the edge is covered with 50% sulfur.

STM images revealed a significantly modified electronic edge structure, which in terms of DFT calculations were shown to be related to two distinct Ni–Mo–S metallic edge states, one of which was similar to that in Co–Mo–S and the other which had no Co–Mo–S or MoS_2 counterpart. The smaller dodecagonal-shaped type B Ni–Mo–S clusters are terminated by three different types of edges. One of these edge types is exactly the same as the fully Ni-substituted Ni–Mo–S($\bar{1}010$) edge in larger clusters. STM images showed that the other two edges also have Ni atoms substituted at Mo edge sites. One of these is a Ni–Mo–S($10\bar{1}0$) edge type that differs from the Ni–Mo–S($10\bar{1}0$) edge in the larger particles. The type B Ni–Mo–S($10\bar{1}0$) edge underwent partial substitution of Mo by Ni, and sulfur adsorption occurred in only parts of the edge with alternating Mo–Ni sections. The last type of edges in type B Ni–Mo–S is associated with high-index ($11\bar{2}0$) edge. These edge types are normally not considered to be stable edge terminations in the literature, but the STM experiments show that such edges may be exposed under equilibrium conditions in the type B Ni–Mo–S structures.

Previous spectroscopic and activity correlation studies of unpromoted and Co- and Ni-promoted catalysts have provided evidence of the existence of different types of MoS_2, Co–Mo–S, and Ni–Mo–S structures [5]. Differences such as those observed in type I and type II Co–Mo–S structures have been shown to be related to differences in the interaction between the sulfide structure and support. Recent DFT calculations [37,76] and STM experiments [43] have provided a better atomistic understanding of support interactions. However, it should be stressed that the type A Ni–Mo–S and type B structures observed in the present study have different intrinsic properties which are not related to support interactions or stacking effects of the MoS_2 layers. Ni is observed to be located at different types of sites in the two types of structures, and, therefore, they are also expected to have very different chemical and catalytic properties. A key goal of future studies will be to achieve a better understanding of these differences, and

such new insight may lead to a better understanding of HDS, HDN and HDY selectivities as a function of the promoter type.

Acknowledgments

This work was supported by the Danish Ministry of Science, Technology, and Innovation through the iNANO center. J.V.L. acknowledges support from the Carlsberg Foundation. Fruitful discussions with Alfons Molenbroek and Anna Maria Puig Molina are gratefully acknowledged.

Supplementary material

The online version of this article contains additional supplementary material.

Please visit DOI: 10.1016/j.jcat.2007.04.013.

References

[1] K.G. Knudsen, B.H. Cooper, H. Topsøe, Appl. Catal. A 189 (1999) 205.
[2] C. Song, X. Ma, Appl. Catal. B 41 (2003) 207.
[3] I.V. Babich, J.A. Moulijn, Fuel 82 (2003) 607.
[4] D.D. Whitehurst, T. Isoda, I. Mochida, Adv. Catal. 42 (1998) 345.
[5] H. Topsøe, B.S. Clausen, F.E. Massoth, in: J.R. Anderson, M. Boudart (Eds.), Catalysis—Science and Technology, vol. 11, Springer-Verlag, Berlin–Heidelberg, 1996.
[6] T. Kabe, A. Ishihara, W. Qian, Hydrodesulfurization and Hydrogenation—Chemistry and Engineering, Wiley–VCH, Kodansha, 1999.
[7] R. Prins, in: G. Ertl, H. Knözinger, J. Weitkamp (Eds.), Handbook of Heterogeneous Catalysis, vol. 4, VHC, Weinheim, 1997, p. 1908.
[8] R. Prins, Adv. Catal. 46 (2002) 399.
[9] B.S. Clausen, S. Mørup, H. Topsøe, R. Candia, J. Phys. 37 (1976) 249.
[10] R. Prins, V.H.J. de Beer, G. Somorjai, Catal. Rev. Sci. Eng. 31 (1989) 1.
[11] P. Gajardo, P. Grange, B. Delmon, J. Catal. 63 (1980) 201.
[12] T.G. Parham, R.P. Merrill, J. Catal. 85 (1984) 295.
[13] M. Karroua, P. Grange, B. Delmon, Appl. Catal. 50 (1989) L5.
[14] M.W.J. Craje, S.P.A. Louwers, V.H.J. de Beer, R. Prins, A.M. Vanderkraan, J. Phys. Chem. 96 (1992) 5445.
[15] R. Chianelli, M. Daage, M. Ledoux, Adv. Catal. 40 (1994) 177.
[16] R. Leliveld, A. van Dillen, J. Geus, D.C. Koningsberger, J. Catal. 175 (1998) 108.
[17] A.M. de Jong, V.H.J. de Beer, J.A.R. van Veen, J.W. Niemantsverdriet, J. Vac. Sci. Technol. A 15 (1997) 1592.
[18] H. Topsøe, B.S. Clausen, R. Candia, C. Wivel, S. Mørup, J. Catal. 68 (1981) 433.
[19] N.-Y. Topsøe, H. Topsøe, J. Catal. 84 (1983) 386.
[20] C. Wivel, R. Candia, B.S. Clausen, S. Mørup, H. Topsøe, J. Catal. 68 (1981) 453.
[21] M. Salmeron, G. Somorjai, A. Wold, R. Chianelli, K. Liang, Chem. Phys. Lett. 90 (1982) 105.
[22] K. Tanaka, Adv. Catal. 33 (1985) 99.
[23] R.R. Chianelli, A.F. Ruppert, S.K. Behal, B.H. Kear, A. Wold, R. Kershaw, J. Catal. 92 (1985) 56.
[24] H. Topsøe, B.S. Clausen, Catal. Rev. Sci. Eng. 26 (1984) 395.
[25] O. Sørensen, B.S. Clausen, R. Candia, H. Topsøe, Appl. Catal. 13 (1985) 363.
[26] Y. Okamoto, T. Kubota, Catal. Today 86 (2003) 31.
[27] Y. Okamoto, M. Kawano, T. Kawabata, T. Kubota, I. Hiromitsu, J. Phys. Chem. B 109 (2005) 288.
[28] T. Shido, R. Prins, J. Phys. Chem. B 102 (1998) 8426.
[29] W. Niemann, B.S. Clausen, H. Topsøe, Catal. Lett. 4 (1990) 355.
[30] S.M.A.M. Bouwens, J.A.R. van Veen, D.C. Koningsberger, V.H.J. de Beer, R. Prins, J. Phys. Chem. 95 (1991) 123.
[31] S. Louwers, R. Prins, J. Catal. 133 (1992) 94.
[32] L.S. Byskov, J.K. Nørskov, B.S. Clausen, H. Topsøe, J. Catal. 187 (1999) 109.
[33] L.S. Byskov, J.K. Nørskov, B.S. Clausen, H. Topsøe, Catal. Lett. 64 (2000) 95.
[34] P. Raybaud, J. Hafner, G. Kresse, S. Kasztelan, H. Toulhoat, J. Catal. 190 (2000) 128.
[35] A. Travert, H. Nakamura, R. van Santen, S. Cristol, J. Paul, E. Payen, J. Am. Chem. Soc. 124 (2002) 7084.
[36] M.Y. Sun, A.E. Nelson, J. Adjaye, J. Catal. 226 (2004) 32.
[37] B. Hinnemann, J.K. Nørskov, H. Topsøe, J. Phys. Chem. B 109 (2005) 2245.
[38] H. Schweiger, P. Raybaud, H. Toulhoat, J. Catal. 212 (2002) 33.
[39] J.V. Lauritsen, S. Helveg, E. Lægsgaard, I. Stensgaard, B.S. Clausen, H. Topsøe, F. Besenbacher, J. Catal. 197 (2001) 1.
[40] S. Helveg, J.V. Lauritsen, E. Lægsgaard, I. Stensgaard, J.K. Nørskov, B.S. Clausen, H. Topsøe, F. Besenbacher, Phys. Rev. Lett. 84 (2000) 951.
[41] J.V. Lauritsen, M.V. Bollinger, E. Lægsgaard, K.W. Jacobsen, J.K. Nørskov, B.S. Clausen, H. Topsøe, F. Besenbacher, J. Catal. 221 (2004) 510.
[42] J.V. Lauritsen, M. Nyberg, J.K. Nørskov, B.S. Clausen, H. Topsøe, E. Lægsgaard, F. Besenbacher, J. Catal. 224 (2004) 94.
[43] J. Kibsgaard, J.V. Lauritsen, B.S. Clausen, H. Topsøe, F. Besenbacher, J. Am. Chem. Soc. 128 (2006) 13950.
[44] V. LaVopa, C. Satterfield, J. Catal. 110 (1988) 375.
[45] M. Egorova, R. Prins, J. Catal. 241 (2006) 162.
[46] J.V. Lauritsen, M. Nyberg, R.T. Vang, M.V. Bollinger, B.S. Clausen, H. Topsøe, K.W. Jacobsen, F. Besenbacher, E. Lægsgaard, J.K. Nørskov, F. Besenbacher, Nanotechnology 14 (2003) 385.
[47] F. Besenbacher, Rep. Prog. Phys. 59 (1996) 1737.
[48] T.H. Cai, Z. Song, J.A. Rodriguez, J. Hrbek, J. Am. Chem. Soc. 126 (2004) 8886.
[49] M.M. Biener, J. Biener, C.M. Friend, J. Chem. Phys. 122 (2005) 034706.
[50] J.V. Barth, H. Brune, G. Ertl, R. Behm, Phys. Rev. B 42 (1990) 9307.
[51] B. Voigtländer, G. Meyer, N.M. Amer, Phys. Rev. B 44 (1991) 10354.
[52] D.D. Chambliss, R.J. Wilson, S. Chiang, Phys. Rev. Lett. 66 (1991) 1721.
[53] J.A. Meyer, I. Baikie, E. Kopatzki, R.J. Behm, Surf. Sci. 365 (1996) L647.
[54] M.V. Bollinger, K.W. Jacobsen, J.K. Nørskov, Phys. Rev. B 67 (2003) 085410.
[55] M.V. Bollinger, J.V. Lauritsen, K.W. Jacobsen, J.K. Nørskov, S. Helveg, F. Besenbacher, Phys. Rev. Lett. 87 (2001) 196803.
[56] L.S. Byskov, B. Hammer, J.K. Nørskov, B.S. Clausen, H. Topsøe, Catal. Lett. 47 (1997) 177.
[57] S.R. Bahn, K.W. Jacobsen, Comput. Sci. Eng. 4 (2002) 56.
[58] B. Hammer, L.B. Hansen, J.K. Nørskov, Phys. Rev. B 59 (1999) 7413.
[59] H.J. Monkhorst, J.D. Pack, Phys. Rev. B 13 (1976) 5188.
[60] K. Laasonen, A. Pasquarello, R. Car, C. Lee, D. Vanderbilt, Phys. Rev. B 47 (1993) 10142.
[61] D. Vanderbilt, Phys. Rev. B 41 (1990) 7892.
[62] N. Troullier, J.L. Martins, Phys. Rev. B 43 (1991) 1993.
[63] J. Perdew, J. Chevary, S. Vosko, K. Jackson, M. Pederson, D. Singh, C. Fiolhais, Phys. Rev. B 46 (1992) 6671.
[64] H. Schweiger, P. Raybaud, G. Kresse, H. Toulhoat, J. Catal. 207 (2002) 76.
[65] S. Cristol, J.F. Paul, E. Payen, D. Bougeard, S. Clémendot, F. Hutschka, J. Phys. Chem. B 106 (2002) 5659.
[66] J. Tersoff, D.R. Hamann, Phys. Rev. Lett. 50 (1983) 1998.
[67] J.V. Lauritsen, J. Kibsgaard, S. Helveg, H. Topsøe, B.S. Clausen, F. Besenbacher, Nat. Nanotechnol. 2 (2007) 53.
[68] S. Kasztelan, H. Toulhoat, J. Grimblot, J. Bonnelle, Appl. Catal. 13 (1984) 127.
[69] B.S. Clausen, B. Lengeler, R. Candia, J. Als-Nielsen, H. Topsøe, Bull. Soc. Chim. Belg. 90 (1981) 1249.
[70] H. Topsøe, R. Candia, N.-Y. Topsøe, B.S. Clausen, Bull. Soc. Chim. Belg. 93 (1984) 783.

[71] S. Bouwens, D.C. Koningsberger, V.H.J. de Beer, S.P.A. Louwers, R. Prins, Catal. Lett. 5 (1990) 273.
[72] S. Bouwens, N. Barthe-Zahir, V.H.J. de Beer, R. Prins, J. Catal. 131 (1991) 326.
[73] B.S. Clausen, H. Topsøe, Hyperfine Interact. 47–48 (1989) 203.
[74] J.T. Miller, W.J. Reagan, J.A. Kaduk, C.L. Marshall, A.J. Kropf, J. Catal. 193 (2000) 123.
[75] J.T. Miller, C.L. Marshall, A.J. Kropf, J. Catal. 202 (2001) 89.
[76] C. Arrouvel, M. Breysse, H. Toulhoat, P. Raybaud, J. Catal. 232 (2005) 161.